Ligand Length and Surface Curvature Modulate Nanoparticle Surface Heterogeneity and Electrostatics

Dongyue Liang,[†] Udaya Dahal,[‡] Meng Wu,[¶] Catherine J. Murphy,[¶] and Qiang Cui[*,§]

†*Department of Chemistry and Theoretical Chemistry Institute, University of Wisconsin-Madison, 1101 University Avenue, Madison, WI 53706*

‡*Department of Chemistry, Boston University, 590 Commonwealth Avenue Boston, MA 02215*

¶*Department of Chemistry, University of Illinois at Urbana-Champaign, Urbana, Illinois 61801, United States*

§*Departments of Chemistry, Physics and Biomedical Engineering, Boston University, 590 Commonwealth Avenue Boston, MA 02215*

E-mail: qiangcui@bu.edu,Tel:(+1)-617-353-6189

Abstract

Motivated by the recent Nuclear Magnetic Resonance (NMR) analysis of functionalized gold nanoparticles (*J. Am. Chem. Soc.*, **2019**, *141*, 4316-4327), we conduct explicit solvent atomistic simulations to characterize the conformational distribution and dynamics of surface ligands on a small gold nanoparticle of 2 nm diameter. Several quaternary alkyl amines are studied to probe the effect of chain length, and a gold slab system is studied to probe the effect of surface curvature. The simulations observe a higher degree of spatial heterogeneity as the ligand length increases, leading to a higher degree of local clustering of longer ligands. Due to the charged nature of the head groups, however, the degree of "ligand bundling" is minimal compared to previous studies of nanoparticles functionalized with charge-neutral ligands. Due to the considerable flexibility of long ligands, their local clustering is not long-lived and rearranges at the time scale of one to ten nanoseconds, suggesting that rearrangements of ligand conformation are unlikely to represent the kinetic bottleneck for nanoparticle-(bio)molecular interactions. The head group methyl proton T_2 relaxation time is computed using a model free approach, and the results are in general agreement with experimental data, providing essential validation of the nanoparticle model and the simulation protocol. Analysis of contributions to the computed T_2 relaxation time suggests that to characterize the time scale of surface ligand dynamics, such measurements should focus on nanoparticles whose hydrodynamic radii are no larger than 3 nm; for larger particles, surface features such as ligand flexibility and heterogeneity can be qualitatively reflected through order parameters and T_2/T_2^*. Non-equilibrium molecular dynamics simulations show that conformational features of the ligands impact the electrostatic properties of the nanoparticle, which suggests that nanoparticle/(bio)molecular interactions can be modulated by perturbing the conformational ensemble of surface ligands.

1 Introduction

Motivated by application, nanoparticles are often coated with specific ligands. For example, to avoid aggregation due to favorable van der Waals interactions,[1] nanoparticles are coated with either charged small molecule ligands or polymers, which can be covalently grafted[2] or attached via non-covalent interactions.[3] Determination of the conformational properties of the coating ligands is therefore an important step towards understanding, and ultimately controlling, how surface coating impacts the interaction between nanoparticle and surrounding (bio)molecules.[4–6]

In the experimental community, recent developments have made it possible to characterize the surface properties of nanoparticles with increasing resolution in both spatial and temporal dimensions. For example, Stellaci and co-workers have demonstrated the use of small angle neutron scattering[7] and mass spectrometry[8] to characterize the ligand distributions on the surface of nanoparticles at near-atomic resolution. A combination of NMR and DFT calculations was able to determine the atomic structure of a small gold nanoparticle functionalized with para-mercaptobenzoic acid.[9] Going beyond static structures, NMR experiments in conjunction with classical molecular dynamics simulations have been used to characterize the conformational ensemble of charge-neutral ligands on the surface of gold nanoparticles;[10] it was shown that transient pockets were formed and could trap small molecule analytes with distinct specificity. For polymer ligands, NMR relaxation measurements demonstrated that poly allylamine hydrochloride (PAH) grafted onto the surface of nano diamond exhibited two populations with distinct conformational flexibilities,[11] suggesting that PAH forms loop structures on the nanoparticle surface[12–14] rather than wrapping tightly around the nanoparticle.

It should be noted that NMR studies of nanoparticles are, in fact, challenging due to the low signal sensitivity associated with particles of small size.[15] Therefore, tight integration of NMR and computational studies for detailed analysis of nanoparticle ligand properties remains an emerging area that warrants in-depth explorations. On one hand, computations are required to help interpret trends observed in the NMR experiments at the molecular level. On the other hand, (semi-)quantiative comparison between computation and experimental measurements provides important calibration of the computational model of nanoparticles. The calibration step is particularly essential considering the complexity of nanoparticle/biomolecule interactions.[16]

In this study, we are specifically motivated by the recent NMR study of Wu et al.,[17] who characterized the distribution and conformation of (16-mercaptohexadecyl)trimethylammonium bromide (MTAB) ligands on the surface of gold nanoparticles and nanorods of different sizes. It was observed that the densities of MTAB were higher at surfaces of larger curvature, an observation consistent with the idea that ligands better avoid each other sterically at curved surfaces and therefore are able to pack with higher densities. Moreover, packing at curved surfaces exhibited a higher degree of disorder or spatial heterogeneity, as revealed by the larger difference between measured T_2 and T_2^* relaxation times for smaller nanoparticles. This feature was qualitatively captured by molecular dynamics simulations, which revealed that ligands on the surface of small nanoparticles tended to form bundles or "islands", while ligands on larger nanoparticles exhibited more homogeneous distributions. The formation of bundles on small nanoparticles was an interesting observation because it led some ligands to expose hydrophobic surfaces, which were suggested to be active in capturing and stabilizing lipid molecules from liposomes,[18] similar to the discussion of lipid capture by hydrophobic nanomaterials such as graphene.[19]

The formation of bundles by long ligands on nanoparticle surface has been observed in previous molecular simulations[20–22] and the finding was rationalized in terms of favorable packing of the hydrophobic segments; for short chains (e.g., up to $-(CH_2)_9$), the small free volume for each chain favors a uniform, symmetric distribution, while for long chains (e.g., $-(CH_2)_{17}$), the larger free volume per chain drives the ligands to distribute asymmetrically to minimize the amount of exposed hydrophobic area.[21] For charged ligands like MTAB, both hydrophobic packing and charge-charge interactions need to be well described, which requires explicit solvent simulations. The molecular dynamics simulations reported in Ref. 17 were conducted using a relatively simple implicit solvent model in which electrostatic interactions were scaled uniformly by the dielectric constant of water, thus the balance between hydrophobic packing and electrostatic interactions might not have been optimally treated; as a result, no quantitative comparison was made between the computation and NMR measurement.

As a follow up study, we conduct explicit solvent molecular dynamics simulations for the similar gold nanoparticles and analyze both the conformational distribution and dynamics of surface ligands; an explicit comparison to the NMR relaxation measurement is made by computing T_2 via a model free approach well established in the biophysics community.[23–25] To probe the effect of surface curvature, we compare the results for a small gold nanoparticle with those for a gold slab; since the packing effect discussed in previous work[20–22] is expected to be sensitive to chain length, we also compare several ligands with hydrophobic segments of variable lengths. Finally, we explore how the conformational characteristics of surface ligands impact electrostatic properties of nanoparticles by computing their mobilities via non-equilibrium molecular dynamics simulations; the results highlight that conformations of surface ligands are crucial to the surface potential of nanoparticles and therefore their interaction with other molecules.[26]

In the following, we first summarize the computational model and simulation details. We then present the results on the conformational and electrostatic properties of different nanoparticle systems; connection to available experimental data is made whenever possible. We end with a few concluding remarks.

2 Computational Methods

2.1 Model setup and molecular dynamics simulations

In this work, we study 2-nm-diameter spherical gold nanoparticles functionalized with alkyl quaternary amine ligands of different lengths (Table 1, also see Scheme 1); a faceted particle model is also studied and exhibit similar results as shown in the **Supporting Information** (Fig. S11). Each nanoparticle is functionalized with 65 butyl trimethyl amine (C4Q), undecyl trimethyl amine (C11Q) or MTAB ligands, thus the ligand density is $\sim$5.2 ligand/nm^2, which is comparable to the value measured for small gold nanoparticles (diameter$<$5 nm);[17] these particles are referred to as C4Q65, C11Q65 and MTAB65, respectively. To probe the effect of curvature, we also study a MTAB functionalized (111) gold slab; the dimension of the slab in the unit cell is 40.8 Å$\times$ 40.8 Å and contains 100 ligands, leading to a ligand density $\sim$3.0 ligand/nm^2, again similar to that measured experimentally for large gold nanoparticles (diameter $>$ 20 nm).[17] The slab has a thickness of 16.3 Å and is decorated with ligands on both sides to avoid asymmetric electric double layers on the two surfaces. Unless specified otherwise, each nanoparticle is solvated with a $120 \times 120 \times 120$ Å^3 water box, and the slab is solvated with a $40.8 \times 40.8 \times 160$ Å^3 box. NaCl of 0.15 M concentration is added with the Monte Carlo displacement method, and the SLTCAP approach[27] is applied for ion number estimates. Following NPT equilibration, the bulk NaCl concentration is approximately 0.15M and 0.10M for the nanoparticle and slab systems, respectively.

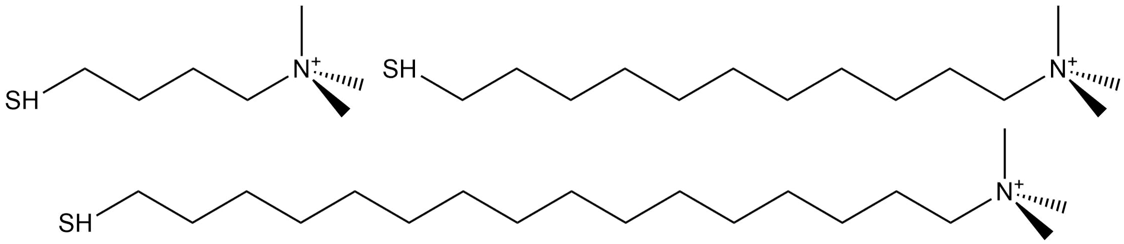

Scheme 1: Ligands used to functionalize the gold nanoparticle in the current study: HS-C4Q, HS-C11Q and HS-MTAB, see Table 1 for chemical formula.

The CHARMM36[28–31] force field is applied to ligands, water and ions. The INTERFACE force field[32] is applied to gold atoms, which are bonded with nearest gold atoms with a force constant of 1000 kcal·mol^{-1}·Å^{-2}; each thiol ligand is covalently bonded to one surface gold atom with a Au–S single bond with a force constant of 200 kcal·mol^{-1}·Å^{-2}. The NAMD package[33] is used for all the molecular dynamics simulations reported in this work. The Particle-mesh-Ewald method[34] is applied for calculating electrostatic interactions, and a grid size of 128 in each spatial dimension is used for the nanoparticle systems, while a 68 × 68 × 168 grid is applied for the slab case. Switching with a switch distance of 10.0 Å and a cutoff of 12.0 Å is applied for the van der Waals interactions. RATTLE[35] is applied to constrain bonds involving hydrogen atoms, enabling the use of a 2 fs integration time step. The Langevin thermostat[36] with a damping coefficient of 1 ps^{-1} is applied to maintain the temperature at 300 K, and the Langevin pressure control[37] is applied during NPT equilibrations with a target pressure of 1.01325 bar. The length of each production run is 80 ns, which is observed to yield adequate convergence for the properties of interest in this work (see **Supporting Information** for examples).

Table 1: Model ligands used in this study.[a]

Model ligand	Chemical formula
C4Q	$-S(CH_2)_4N(CH_3)_3^+$
C11Q	$-S(CH_2)_{11}N(CH_3)_3^+$
MTAB	$-S(CH_2)_{16}N(CH_3)_3^+$

a. Each gold nanoparticle is functionalized with 65 ligands with a ligand density of 5.2 ligand/nm^2; thus the functionalized particles are referred to as C4Q65, C11Q65 and MTAB65. The gold slab is functionalized on both sides with 100 MTAB ligands in total with a ligand density of 3.0 ligand/nm^2. Note that these quaternary amine ligands are not titratable.

2.2 Computation of T_2 relaxation time

We apply similar methodology as Riccardi et al.[38] to compute the T_2 relaxation time, except that we study methyl proton relaxation time in the MTAB head group as was done in the experimental work of Wu et al.;[17] the experimental data are summarized in Table S1 in the **Supporting Information**. The T_2 relaxation time can be calculated with the following expression (not including contribution from chemical shift anisotropy):[23,24]

$$T_2^{-1} = \frac{d}{8}[9J(\omega_H) + 6J(2\omega_H) + 5J(0)], \tag{1}$$

where $d = \frac{\mu_0^2\hbar^2}{4\pi^2}\frac{\gamma_H^4}{r_{HH}^6}$, $J(\omega)$ the spectral density, μ_0 the vacuum permeability, $\hbar$ the reduced Plank constant, γ_H is the gyromagnetic ratio, r_{HH} the equilibrium average H-H distance; ω_H is experimental Larmor frequency of H ($2\pi\times500.13$ MHz). The equation considers the fact that two nearby protons for each methyl proton are involved in the dipolar coupling; as shown in Fig. S1 in **Supporting Information**, the protons in other groups are sufficiently far and therefore do not have to be considered in the relaxation mechanism.[39]

The spectral density is defined as:[40]

$$J(\omega) = 2\int_0^{\infty} C(t)cos(\omega t)dt, \tag{2}$$

where $C(t)$ is the time correlation function for the HH unit vector reorientational dynamics: $C(t) = \langle P_2(\vec{\mu}(t)\cdot\vec{\mu}(0))\rangle$, in which P_2 is the second-order Legendre polynomial. Here we apply the model-free approach of Lipari-Szabo,[23] which assumes the decoupling of internal motion and the overall tumbling; i.e. $C(t) = C_{int}(t)C_o(t)$. In practice, $C_{int}(t)$ is evaluated based on motions relative to the gold core of the nanoparticle, and for each ligand, the correlation function is averaged for all the 9 H-Hs on each head group. A double-exponential fit is used as in the Clore model[41] for the first 5 ns of the autocorrelation function (computed using 20 ns MD segments):

$$C_{int}(t) = A_0 + A_f e^{-\frac{t}{\tau_f}} + A_s e^{-\frac{t}{\tau_s}}, \tag{3}$$

in which τ_f and τ_s are the fast and slow correlation times, respectively, and A_0 is also referred to as the order parameter,[23] which measures the ability of the HH pair to sample all possible orientations; the fit is carried out under the constraint of $A_0 + A_f + A_s = 1.0$. The rotational correlation function associated with the overall tumbling is calculated with the Stokes-Einstein relation for rotational diffusion,

$$C_o(t) = \frac{1}{5}e^{-\frac{t}{\tau_R}}, \tag{4}$$

in which $\tau_R = \frac{4\pi\eta r^3}{3k_BT}$; here r is the hydrodynamic radius (*vide infra*). With these models for $C_{int}(t)$ and $C_o(t)$, the spectral density can be integrated analytically as the following:

$$J(\omega) = \frac{2}{5}\left(\frac{A_0\tau_R}{1+(\omega\tau_R)^2} + \frac{A_f\tau'_f}{1+(\omega\tau'_f)^2} + \frac{A_s\tau'_2}{1+(\omega\tau'_s)^2}\right) \tag{5}$$

where $\frac{1}{\tau'_f} = \frac{1}{\tau_f} + \frac{1}{\tau_R}$, and the similar definition applies to τ'_s. The slab model is used to estimate T_2 for large nanoparticles that have a low degree of curvature; for estimating $C_o(t)$, a radius of 5 nm is assumed for the gold core (also see **Supporting Information**).

2.3 Electrophoretic Mobility calculations

Experimentally, electrophoresis measurement is widely applied to characterize the electrostatic properties of nanoparticles.[26,42–44] Along this line, we apply the drift velocity method[31,45,46] to estimate the electrophoretic mobilities of nanoparticles; we chose to focus on mobility rather than electrostatic potential to avoid the difficulty of defining the slipping plane for nanoparticles with long ligands such as MTAB, which leads to highly heterogeneous surfaces (*vide infra*). Under an external electric field, the mobility is computed as:

$$\mu = \frac{v}{E} \tag{6}$$

where v is the drift velocity of the nanoparticle, E the strength of the external electric field. For the drift velocity simulations, the system setups are identical to the equilibrium MD simulations, unless specified otherwise. To compromise between convergence and preservation of the electrical double layer around the charged nanoparticle, an external electric field of 0.05 kcal · mol^{-1} · Å^{-1} · e^{-1} is applied (1 kcal · mol^{-1} · Å^{-1} · e^{-1} = 4.3 × 10^6 V/cm), similar to our recent work.[26] Comparison to Nosé-Hoover thermostat shows that a damping coefficient smaller than 0.02 ps^{-1} is necessary for obtaining the correct magnitude of drift velocity, and a value of 0.02 ps^{-1} is applied in this work. For each case studied, the length of each drift velocity production run is 20 ns, and 6 individual runs are performed with the electric field applied in different directions (±x, ±y, ±z; see Table S2 in **Supporting Information**).

3 Results and Discussion

3.1 Conformations of ligands

Snapshots for the simulated systems are shown in Fig. 1. To characterize the ligand orientation, we plot the angular distribution (properly scaled by the Jacobian factor $sin\theta$) of the vector pointing from the anchoring sulfur atom to the amine nitrogen in Fig. 2a and the radial distribution of the amine nitrogen in Fig. 2b; the 2D joint distributions for the different cases are included in Fig. S2 in the **Supporting Information**. The angular distribution is fairly narrow and peaked at small angles for the short butyl trimethyl amine (C4Q) on the gold nanoparticle and for MTAB on the surface of the gold slab; the latter is similar to observation in previous self-assembled monolayer simulations.[20] Correspondingly, the spatial distribution of the amine nitrogen is narrow for C4Q. These observations are expected since C4Q is short and rigid, while MTAB ligands pack tightly on the flat surface of the gold slab. By contrast, the angular distributions and spatial amine nitrogen distributions are much broader for both undecyl trimethyl amine (C11Q) and MTAB on the gold nanoparticle; the angular distributions also peak around larger values in the 60-70 ° range. For MTAB, the distribution at small angles is even lower in magnitude than C11Q, suggesting that the longer MTAB chains have a higher tendency to be tilted; in fact, there is a notable population with the angle larger than 90 °, which corresponds to MTAB wrapping around the nanoparticle.

To further characterize the spatial distribution of the ligands, we project the position of the amine nitrogen onto the surface of the nanoparticle or slab and average the distribution over the time window of 25 ns. As shown in Fig. 3, the C4Q case leads to the most regular patterns of alternating high and low densities, reflecting the generally rigid orientation of the short ligands. This is also supported by the high degree of similarity between the 2D distributions for the first and last 25 ns of trajectories, which are separated by another 25 ns of simulation; i.e., the 2D distribution is fairly static. The distribution is not as regular for the case of MTAB on the gold slab; this is likely because the ligand density on the slab

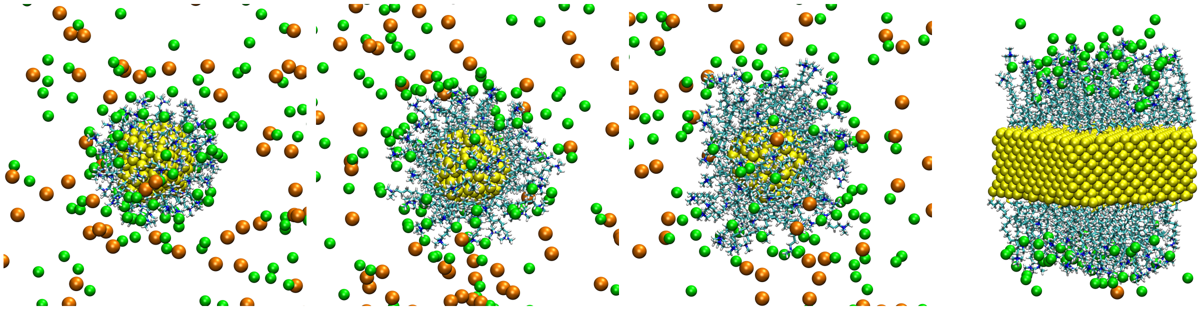

(a) (b) (c) (d)

Figure 1: Snapshots of the functionalized nanoparticles/slab from molecular dynamics simulations. The a-d panels represent C4Q65, C11Q65, MTAB65 and MTAB-slab cases, respectively. For clarity, water molecules are not shown. Color representations of elements: Au - yellow, C - cyan, N - blue, Cl - green, Na - orange.

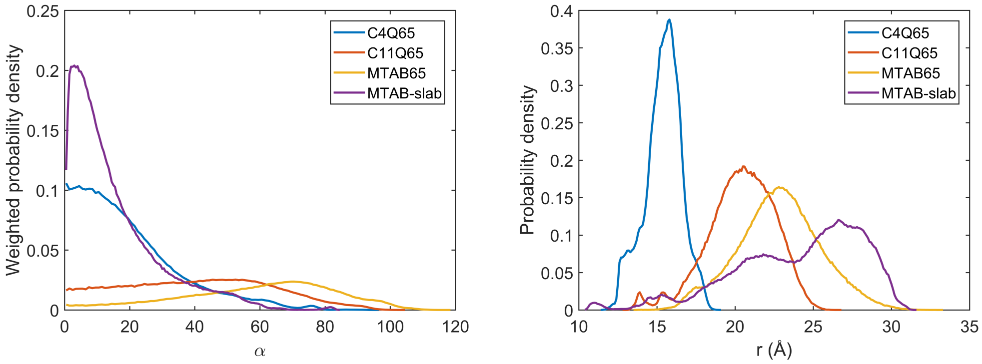

(a) (b)

Figure 2: Ligand distribution on the surface of gold nanoparticles and on the gold slab from 80 ns molecular dynamics simulations. (a) Angular distribution (weighted by the Jacobian $sin\theta$) of the ligand S-N vector relative to the nanoparticle surface normal. (b) Radial distribution of ligand nitrogen; for nanoparticles, r is defined relative to the center of the particle, and for the slab, it is defined along the surface normal and shifted such that the average position of the ligand sulfurs aligns with that in the nanoparticle cases. See Fig. S2 for the 2D joint distributions.

is lower than that for the nanoparticle cases and thus MTAB ligands can, in fact, tilt and pack locally, leading to a limited degree of heterogeneity. Nevertheless, the distribution is fairly static as reflected by the comparison of Figs. 3g and 3h.

By contrast, spatial heterogeneity is evident for the cases of C11Q and MTAB on the gold nanoparticle. For example, Fig. 3e features two large high-density regions, suggesting that MTAB ligands cluster locally, which is reminiscent of the "islands" discussed in Ref. 17. The degree of spatial heterogeneity is evidently higher for MTAB than C11Q (e.g., compare Figs. 3c and e), which supports the previous discussions[20–22] of favorable non-polar packing that promotes a non-homogeneous distribution of ligands on curved surfaces. The difference between the packing of short and long ligands is also made clear by spherical Voronoi partitioning of the ligand nitrogen distribution averaged over the period of 1 ns (compare panels a-c with d-f in Fig. 4). Moreover, a clustering analysis of ligand nitrogen positions during 25 ns of MD trajectory segment also indicates a higher degree of heterogeneity in cluster size for the longer ligands (C11Q and MTAB) than the shorter C4Q ligand (Fig. S5).

Visual inspection of snapshots (Fig. 1), however, does not reveal as significant bundling as observed in previous studies.[17,20–22] This is because the ligands in the current case are charged and therefore the electrostatic repulsion among the cationic amine groups prevents tight association of different ligands; the reduced degree of asymmetry in ligand distribution was also observed for charged long ligands in a previous study.[21] Comparing the 2D distributions for the first and last 25 ns of trajectories for MTAB65 (Figs. 3e and 3f; also see the shift of red regions in Figs. 4d-f) also suggests that the clustering pattern is not static. For example, the large, high-density region observed in the first 25 ns breaks up into smaller regions during the last 25 ns. The relative ease of rearrangements of ligand clusters is likely facilitated by the intrinsic flexibility of the long MTAB ligands and the charge-charge repulsion among the amine groups. To further quantify the time scale of conformational rearrangements, we next turn to the discussion of dynamical features of the ligands.

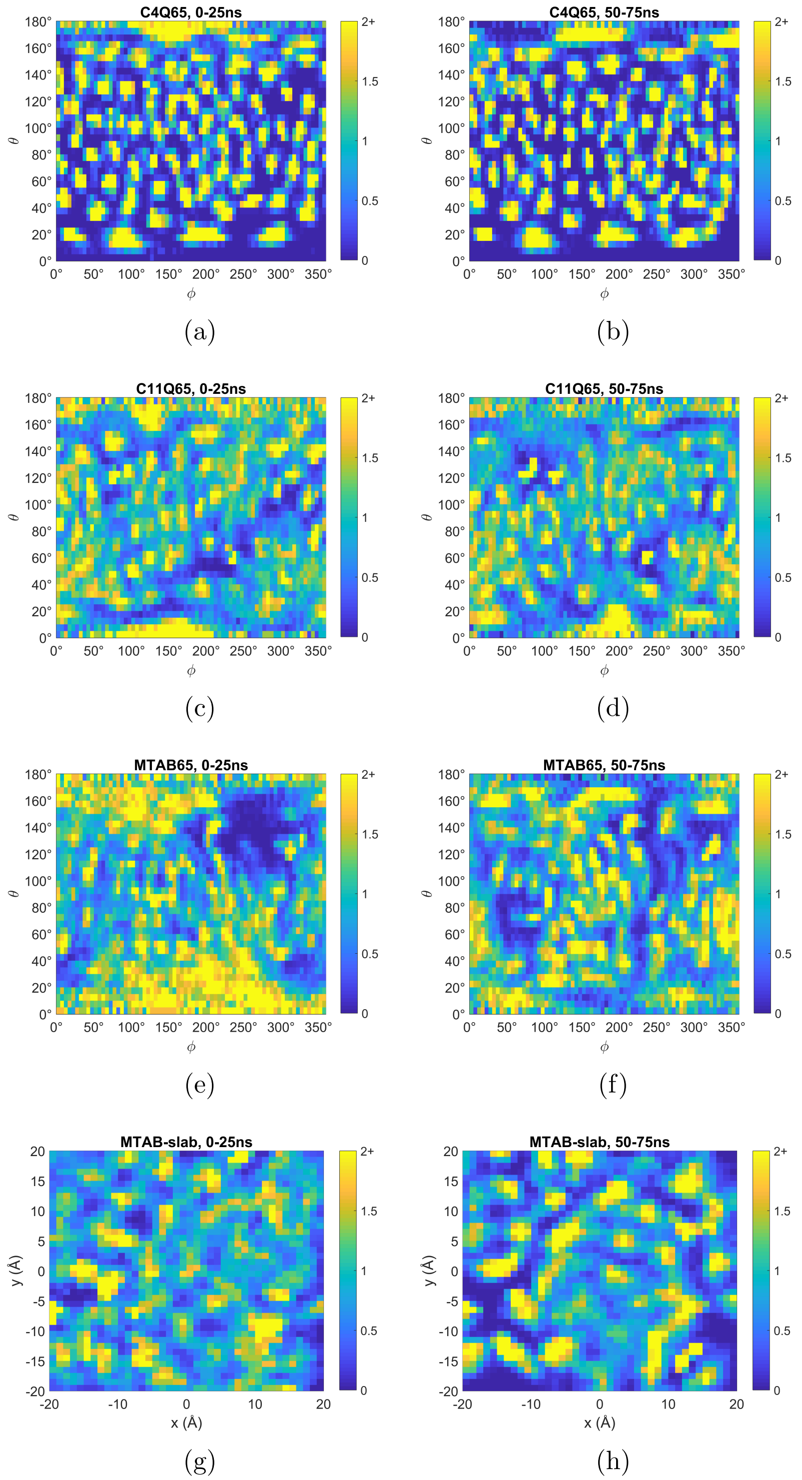

Figure 3: Head-group nitrogen density projected onto (a-f) the surface of functionalized gold nanoparticles or (g-h) the x-y plane for the gold slab; the results are normalized against the average ligand densities and averaged over different 25 ns segments of trajectories. For the gold slab, only ligand on one side of the slab is analyzed. Although the degrees of (ir)regularity can in principle by differentiated by spatial entropy,[47] this is not pursued here; instead, the degree of ligand clustering is characterized by the area spanned by each ligand based on spherical Voronoi tessellation (Fig. 4 and S4).

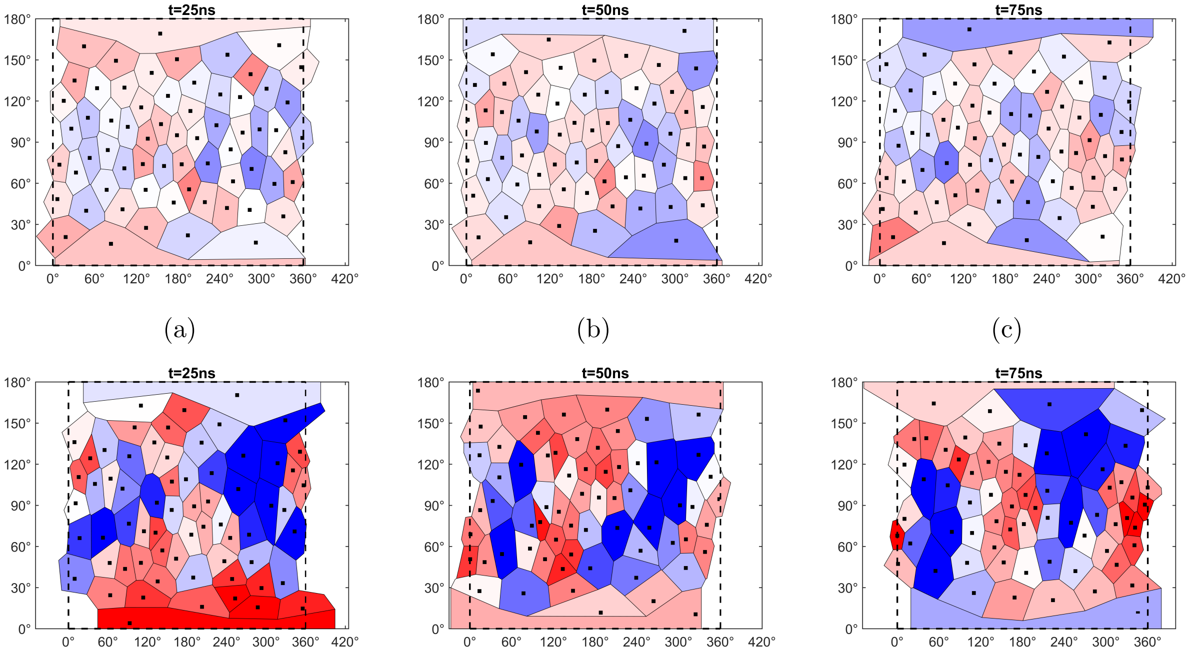

(a) (b) (c)

(d) (e) (f)

Figure 4: Spherical Voronoi tessellation of projected positions of ligand nitrogen to the surfaces of (a-c) C4Q65, (d-f) MTAB65 nanoparticles at t = 25, 50, 75 ns from MD simulation trajectories. Each set of positions is obtained by averaging over 10 frames with 100 ps intervals near the respective time. Each Voronoi region is colored according to the spherical area, where darker blue/red colors represent larger/smaller areas with respect to the average, respectively; the identical color scale is used for all panels. For the results for other cases, see Fig. S4. Spherical Voronoi tessellation and surface projection is done using SciPy1.0.[48]

3.2 Dynamics of ligands

We have computed several types of dynamical characteristics of the ligands in the nanoparticle and slab systems. First, we compute the van Hove function[40,49] of the amine nitrogens; it is defined as,

$$G(\mathbf{r},t) = \frac{1}{N}\langle\sum_{i=1}^{N}\sum_{j=1}^{N}\delta(\mathbf{r}-\mathbf{r}_i(t)+\mathbf{r}_j(0))\rangle. \tag{7}$$

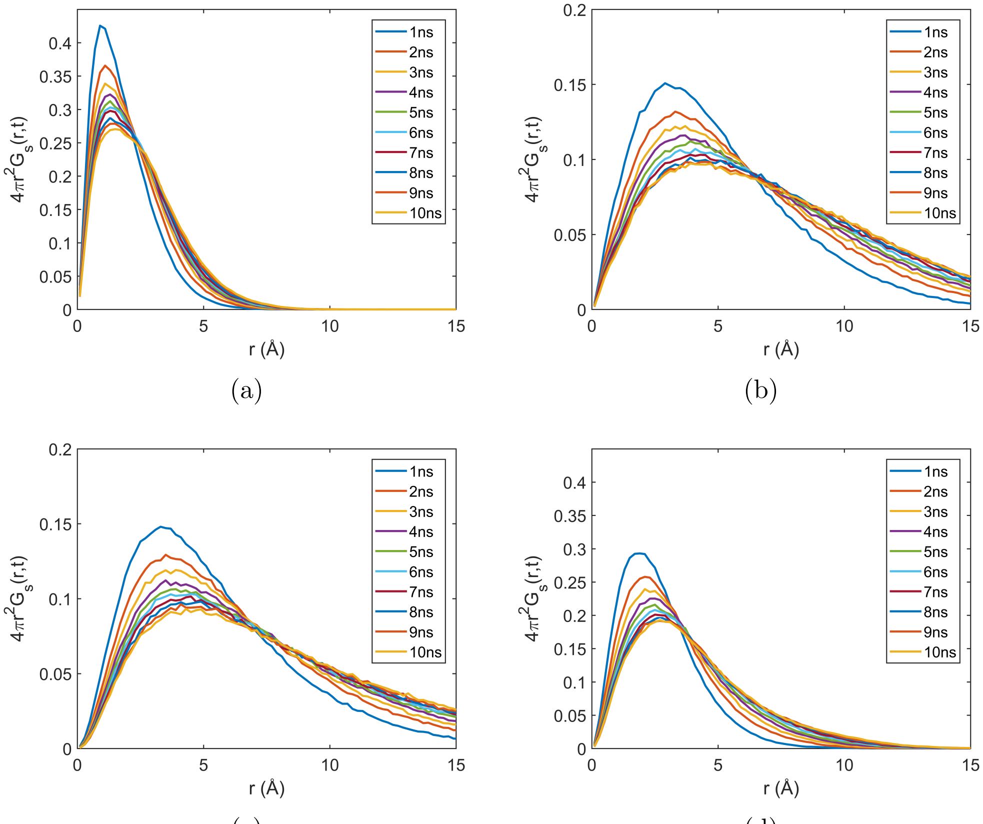

(a) (b)

(c) (d)

Figure 5: The self contribution of van Hove function for ligand head-group nitrogens in (a) C4Q65, (b) C11Q65, (c) MTAB65 and (d) MTAB-slab cases with time intervals of 1, 2, ..., 10 ns.

It's common to separate $G(\mathbf{r},t)$ into self and distinct parts, $G(\mathbf{r},t) = G_s(\mathbf{r},t) + G_d(\mathbf{r},t)$, where

$$G_s(\mathbf{r},t) = \frac{1}{N}\langle\sum_{i=1}^{N}\delta(\mathbf{r}-\mathbf{r}_i(t)+\mathbf{r}_i(0))\rangle, \tag{8}$$

and

$$G_d(\mathbf{r},t) = \frac{1}{N}\langle\sum_{i\neq j}^{N}\delta(\mathbf{r}-\mathbf{r}_i(t)+\mathbf{r}_j(0))\rangle. \tag{9}$$

$G_s(\mathbf{r},t)$ gives the probability that particle i has moved $\mathbf{r}$ over time t, while $G_d(\mathbf{r},t)$ is proportional to the probability that the separation between particle j at time t and particle i at time 0 is $\mathbf{r}$ (note that $\int G_s(\mathbf{r},t)d\mathbf{r} = 1$, while $\int G_d(\mathbf{r},t)d\mathbf{r} = N-1$); $G_d(\mathbf{r},0)$ is nothing but $\rho g(\mathbf{r})$, where ρ is the bulk density and $g(\mathbf{r})$ the pair radial distribution function.

The plots for the radial self part $G_s(r,t)$ at different time scales $(t \leq 10ns)$ are shown in Fig.5. As expected, the amine nitrogen in C4Q is rather static, with $4\pi r^2 G_s(r,t)$ at different time scales closely resembling each other; the range of $4\pi r^2 G_s(r,t)$ in r is also narrow and limited to $r < 5$ Å. The degree of motion for the remaining systems increases in the order of gold slab, C11Q-nanoparticle and MTAB-nanoparticle. For example, for the case of MTAB on the gold nanoparticle, the peak value of $4\pi r^2 G_s(r,t)$ is merely 0.15 for $t = 1\ ns$ and decays significantly to < 0.1 at $t = 10\ ns$; by comparison, $4\pi r^2 G_s(r,t)$ for C4Q has the peak value of >0.4 and ∼0.27 at $t = 1\ ns$ and $t = 10\ ns$, respectively. The range that $4\pi r^2 G_s(r,t)$ spans in r for C11Q and MTAB on nanoparticle is also substantially larger than C4Q and MTAB-slab cases. Evidently, the longer MTAB ligands exhibit a significant degree of mobility on the surface of a nanoparticle.

For characterizing the clustering dynamics, the radial distinct part, $G_d(r,t)$, is more relevant and plotted for the various systems in Fig. 6. The rigid and static nature of C4Q is again well represented by its $G_d(r,t)$ in Fig. 6a; the layered feature in the pair distribution remains largely unchanged as t increases from 0 to 10 ns, and the "correlation hole" at short distance range is barely filled up as t increases. For MTABs on the surface of a gold slab (Fig. 6d), the $G_d(r,t)$ plots also maintain significant features near the peak distance in $G_d(r,0) \propto g(r)$, suggesting that amine nitrogens largely remain separated. Nevertheless, the correlation hole at short distance gets filled up fairly quickly, implying more motions of the MTAB ligands on the slab as compared to C4Q on a nanoparticle. For both C11Q and MTAB on the nanoparticle, $G_d(r,t)$ decays within a few nanoseconds into rather featureless

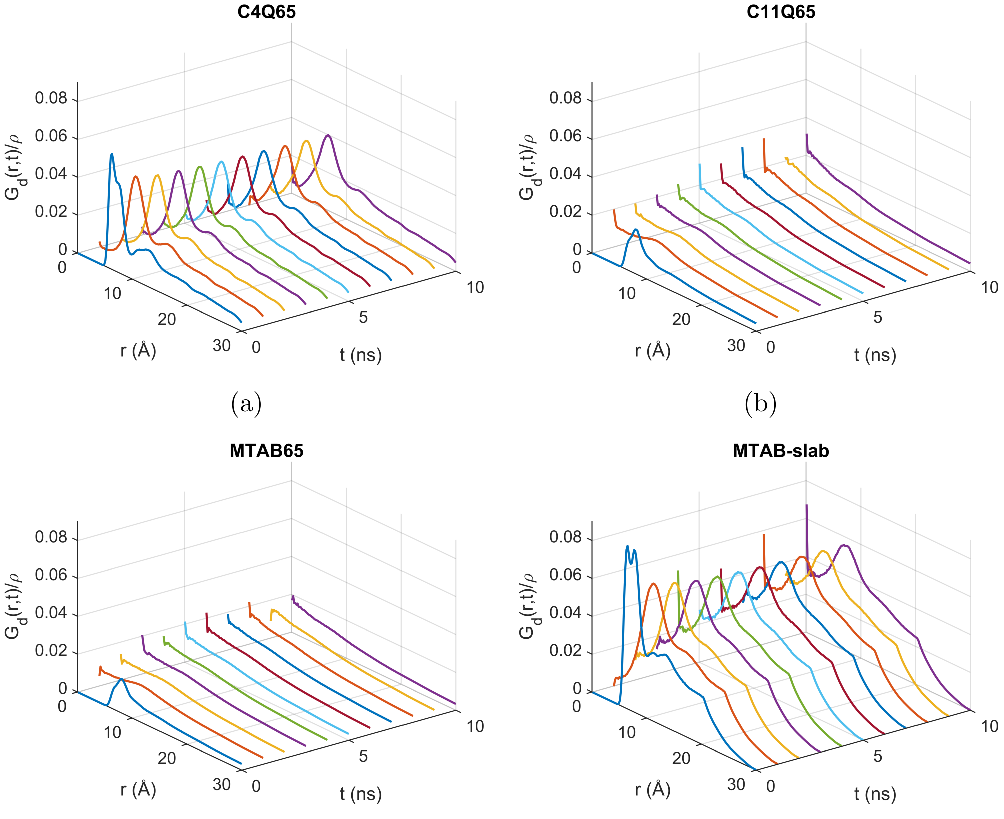

(a) (b) (c) (d)

Figure 6: The distinct contribution of van Hove function for ligand head-group nitrogens in (a) C4Q65, (b) C11Q65, (c) MTAB65 and (d) MTAB-slab cases with time intervals of 0, 1, ..., 10 ns.

curves (Figs. 6b-c). Therefore, these longer ligands exhibit significant motions and there is no obviously persistent pattern in the relative ligand distribution beyond the nanosecond timescale.

To characterize the local ligand dynamics, we have computed the P_2 autocorrelation function of the H-H vectors of the quaternary amine methyl groups; the $C_{int}(t)$ reflects the reorientation dynamics of the methyl groups. An example for $C_{int}(t)$ is presented in Fig. 7a for the case of MTAB65, while the results for other systems are included in the **Supporting Information** (Fig. S6). $C_{int}(t)$ can be fitted into the sum of two exponentials (Eq. 3) with time constants τ_f, τ_s in the range of tens and hundreds of picoseconds, respectively. As shown in Figs.7b-c, there is a considerable breadth of distribution in both τ_f and τ_s for all the systems considered, reflecting the heterogeneity in ligand dynamics due to differences in local environment sampled over the molecular dynamics simulations. In particular, C4Q on the nanoparticle and MTAB on the gold lab exhibit very broad distributions with the time constants varying almost an order of magnitude; this is because ligands in these systems remain rather rigid as revealed by the van Hove function and therefore the methyl groups experience a considerable degree of static (on the time scale of head group reorientation) heterogeneity. By contrast, C11Q and MTAB on the nanoparticle exhibit much narrower distributions centered at the shorter time scales; τ_f is in the range of <10 ps, and τ_s is in the range of ~100 ps. These trends are consistent with the significant degrees of motions for these flexible ligands on a curved surface as reflected by the van Hove functions; i.e., ligand flexibility reduces the impact of local environment, as discussed for motional narrowing.[50] At a more quantitative level, fitting the τ_s distributions into Γ distributions leads to variances of 6.3×, 1.1×, 0.8× and 1.4×10^4 ps^2 for C4Q65, C11Q65, MTAB65 and MTAB-slab, respectively (Fig. S7).

The differences in ligand flexibility are also illustrated by the long-time behaviors of $C_{int}(t)$, i.e., the order parameter, A_0. As shown in Fig. S6, while finite values of A_0 are often observed for ligands in C4Q and MTAB-slab, most $C_{int}(t)$ for MATB65 decays to essentially

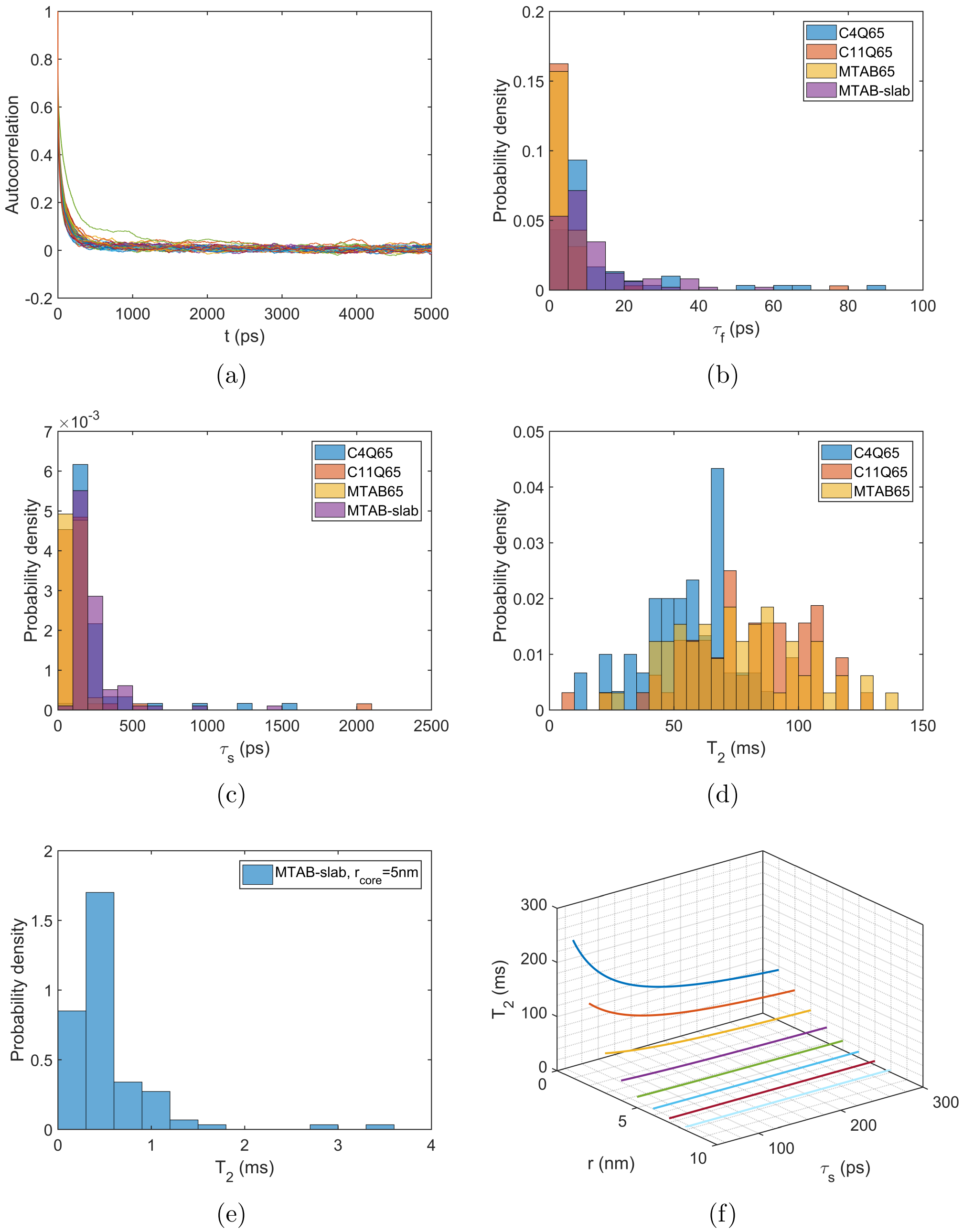

Figure 7: Dynamics and T_2 relaxation time of ligand head group methyl protons from MD simulations. (a) Computed P_2 H-H correlation function, $C_{int}(t)$, for the MTAB head group methyl protons in the MTAB65 system computed from a 20 ns trajectory segment; the different lines indicate results for different methyl protons averaged over each ligand; for $C_{int}(t)$ of other cases, see Fig. S6. (b) Distribution of the fast (τ_f) and slow (τ_s) time scales obtained by a double-exponential fit of $C_{int}(t)$ (Eq. 3); each $C_{int}(t)$ used for fitting is first averaged over the 9 H-Hs in the same ligand. (d-e) Distribution of computed T_2 relaxation time (Eq. 1) for different nanoparticles and the gold slab, which mimics a large gold nanoparticle with the core radius of 5 nm. See text for the discussion of nanoparticle radii used in the calculations. (f) T_2 relaxation time calculated with different slow time scales (τ_s) and hydrodynamic radii (r that determines τ_R in Eq.4) with the model free approach. Here the other parameters from double exponential fit take constant values based on MTAB65: $A_f = 0.58$, $A_s = 0.41$, $\tau_s = 4$ ps, $A_0 = 0.01$). The experimental T_2 values are 20±2 ms, 9.8±1.0 ms and 2.4±0.3 ms for MTAB-gold nanoparticles of core diameters of 1.2±0.3 nm, 4.8±1.1 nm and 10.8±0.8 nm, respectively (Table S1).

zero (Fig. 7a), suggesting that the head groups in MATB65 are able to sample all orientations, while those in C4Q and MTAB-slab may experience a more confining environment (for a distribution of A_0, see Fig. S8b).

Before discussing the results for the computed T_2 relaxation time, we note that the rotational contribution is expected to be significant, as discussed below. Therefore, it is important to choose the proper effective nanoparticle size when evaluating the rotational correlation time using the Stokes-Einstein relation. In the original work of Wu et al.,[17] hydrodynamic radii for the nanoparticles were measured using dynamic light scattering, and it was observed that the hydrodynamic radii are significantly larger than the core size of the particles observed using transmission electron microscopy; for small particles, the ratio was approximately three (see Fig. S8a), indicating either strongly coupled water layers or a minor degree of aggregation in solution. Therefore, for the case of MTAB65, we used this ratio of 3.1 to estimate the hydrodynamic radius based on its core size (1 nm); for C4Q65 and C11Q65, we scale down from the estimated hydrodynamic radius of MTAB65 based on the peak positions of ligand nitrogen distributions computed from MD simulations (Fig. 2b); to mimic a large nanoparticle using ligand dynamics results for MTAB-slab, we use an arbitrary large core radius of 5 nm (Ref. 17 analyzed nanoparticles of core radius between 0.6 and 12.5 nm), and scale by the ratio of 3.1 to obtain an estimate of its hydrodynamic radius.

With the computed ligand reorientation time scales (τ_f, τ_s) and estimated rotational correlation time (τ_R), the computed T_2 relaxation times are shown in Fig. 7d. The computed T_2 values for the nanoparticle ligands feature considerable spreads, although the average values for ligands in the three particles are all ∼50 ms. By contrast, the estimated T_2 values for ligands in a large nanoparticle using MTAB-slab as a model are significantly shorter and the distribution narrowly peaks ∼0.5 ms (Fig. 7e). These general trends compare favorably to the results of experimental NMR relaxation measurements.[17] As summarized in Table S1 in the **Supporting Information**, the measured T_2 values for MTAB on gold nanoparticles of diameter 1.2, 4.8 and 10.8 nm are ∼20, 9.8 and 2.4 ms, respectively. Thus both the order of magnitude of T_2 and its significant dependence on the particle size are consistent between computation and experiment; note that the ligand densities for the MTAB65 and MTAB-slab cases are comparable to those measured in the experimental study,[17] thus the comparison of computed and measured T_2 values is valid.

An important question concerns the motion(s) that contribute significantly to the value of T_2; in particular, to what degree the steep dependence of T_2 on the particle size is due to the overall rotation (tumbling) of the nanoparticle vs. internal ligand flexibility? Numerical analysis of the spectral densities (Eq. 5) indicates that once the hydrodynamic radius passes certain value, the spectral density and therefore the T_2 value is largely dictated by rotational relaxation and no longer sensitive to the time scale of ligand dynamics; this is illustrated in Fig. 7f, which shows that for particles with a hydrodynamic radius beyond 3 nm, the T_2 value is largely insensitive to τ_s; this is further supported by the observation that computed T_2 values for MTABs are not sensitive to either the water model (Fig. S9), thermostat (Fig. S10) or the surface feature of the nanoparticle (Fig. S11). The considerable spread in computed T_2 values for ligands on the same nanoparticle originate largely from the distributions of the order parameter A_0 (see Fig. S8b), which scales the contribution of rotational relaxation to the spectral density (Eq. 5); the distribution of order parameter reflects the heterogeneity in the local environment of the methyl group that determines its ability to reorient. This analysis highlights that to probe dynamics of flexible ligands (i.e., τ_s rather than A_0) with T_2, it is important to focus on small nanoparticles.

Experimentally, another significant observation was that the difference between T_2 and T_2^*, which were determined by the Carr-Purcell-Meiboom-Gill pulse sequence and proton chemical shift peak width, respectively, was significant for nanoparticles smaller than 13.4 nm (diameter); for example, the corresponding values are ∼9.8 and 1.0 ms for a 4.8 nm nanoparticle, while both values are ∼1.5 ms for a 13.4 nm nanoparticle. This observation was interpreted[17] to reflect the higher degree of conformational disorder of MTAB on the surface of smaller nanoparticles. In our calculations, the degree of spatial heterogeneity (e.g., clustering) and thus variation in the local environment experienced by the head groups (reflected experimentally by chemical shifts) is indeed larger for the case of MTAB65 as compared to MTAB-slab (see Figs. 3 and 4), although our results also highlight the importance of ligand length. Moreover, due to the structural flexibility at curved surfaces, MTAB on the nanoparticle in fact exhibits a narrower distribution in the reorientation dynamics (i.e., τ_s, Fig. 7c) and order parameter (i.e., A_0, Fig. S8b) compared to MTAB on the slab; the observed smaller difference between experimental T_2 and T_2^* for larger nanoparticles, therefore, might be due in part to the fact that contribution from ligand dynamics is largely quenched in those large particles.

3.3 Electrostatic properties

In this subsection, we analyze the electrostatic properties of the nanoparticles; the aim is to understand whether the distinct conformational characteristics of the surface ligands discussed above have any major impact on the electrostatic potential profile of the nanoparticles and thus their interaction with other molecules.[51,52]

Table 2: Mobilities (unit: $10^{-4} \cdot cm^2 \cdot V^{-1} \cdot s^{-1}$) of different nanoparticles from drift velocity simulations.[a]

Nanoparticle	Mobility
C4Q65	9.2 ± 0.4
C4Q65[b]	9.0 ± 0.5
C11Q65[b]	10.8 ± 0.9
MTAB65[b]	11.2 ± 0.9

a. R_g values for the different nanoparticles (including gold core, in Å) are, C4Q65: 9.03 ± 0.01, C11Q65: 10.63 ± 0.04, MTAB65: 11.9 ± 0.1.

b. Computed using a larger box of 15 nm size instead of 12 nm.

For this purpose, we have computed the electrophoretic mobility of the nanoparticles using non-equilibrium molecular dynamics (see Computational Methods and Fig. S12). We chose mobility over a direct computation of electrostatic potential[53] because the nanoparticle surface with long ligands such as MTAB is very heterogeneous, which considerably complicates the analysis and presentation of electrostatic potential. The computed mobilities are summarized in Table 2, which reveals an unexpected observation: the mobility of the larger MTAB functionalized gold particle, in fact, has a significantly (∼20%) *higher* mobility than the particle decorated with the same number (65) of C4Q ligands.

This surprising result can be explained by examining the ion distribution around the particle. In Fig.8a, we plot the apparent charge of the particle, defined as the sum of ligand charge and charges of salt ions, within a given radius from the center of the nanoparticle; the result is normalized with respect to the bare charge of the particle. The somewhat complex features of the apparent charge plot reflects the conformational distribution of the ligands, which lead to distinct distributions of the amine groups around the nanoparticle; as shown in Fig. 2b, the amine distribution is narrow for the short and rigid C4Q, but the distribution is much broader for C11Q and MTAB (Fig.2a). Some of the amine groups in C11Q and MTAB are positioned to be close to the nanoparticle surface and therefore effectively shielded from the counter ions; this observation is generally consistent with the broader chemical shift peaks[54] observed for MTAB on small nanoparticles in Ref. 17. Indeed, the radial distribution of Cl^- around amine nitrogen in Fig. 8b indicates that Cl^- association to amine is substantially lower for C11Q and MTAB as compared to C4Q. This lower level of counter ion compensation leads to higher peak values for the apparent charge plots for C11Q65 and MTAB65, which explain their higher electrophoretic mobility values than C4Q65. This analysis highlights that the conformational characteristics of surface ligands can modify the electrostatic properties of the nanoparticle/solvent interface and therefore are expected to have an impact on the interactions between the nanoparticle and other (bio)molecules.[26]

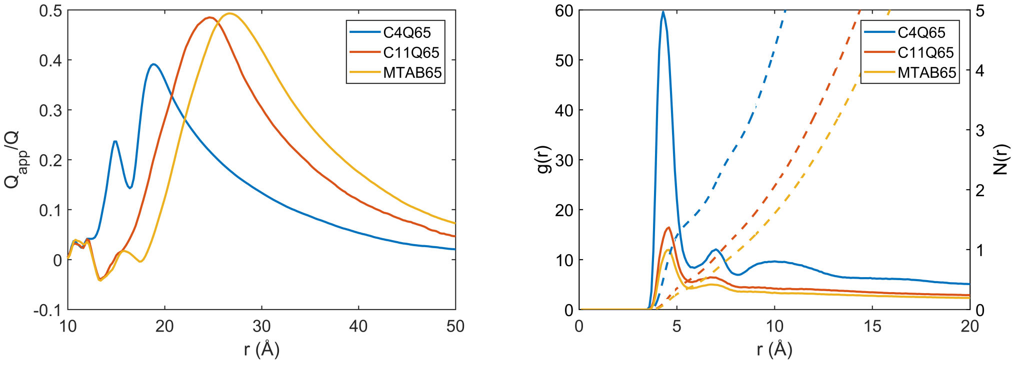

(a) (b)

Figure 8: Apparent charge and ion distribution of different nanoparticles from MD simulations. (a) The ratio of apparent charge (Q_{app}) and bear charge (Q) as a function of distance from the nanoparticle center; $Q_{app}(r)$ included the sum of ligand charge and salt charge up to distance r; for its convergence behavior with respect to sampling time, see Fig. S13. (b) Chloride radial distribution function with respect to ligand head-group nitrogens; the dashed lines are the integrated number of ions as a function of chloride/nitrogen distance.

4 Concluding Remarks

The conformation and dynamics of surface ligands are expected to play a major role in determining how nanoparticles interact with (bio)molecules in solution. Therefore, it is important to characterize these properties and understand factors that modulate them. Along this line, computations and experiments are highly complementary: due to the small size and compositional heterogeneity, nanoparticles are not easy to characterize with atomistic level of detail using experimental techniques alone; on the other hand, the complexity of the nanoparticle/solution interface makes quantitative molecular simulations far from straightforward either. A robust understanding, therefore, requires integration of experimental and computational analyses.

In this study, we analyze the conformation and dynamics of a series of alkyl quaternary amine ligands of different chain lengths on the surface of small (core diameter of 2 nm) gold nanoparticles; to probe the effect of curvature, we also simulate a gold slab functionalized with the MTAB ligand. The ligand densities are comparable to those measured experimentally, making it possible to compare the simulations with recent NMR relaxation measurements on similar systems.[17]

In terms of conformational distribution of the ligands, the simulations observe a higher degree of spatial heterogeneity as the ligand length increases, leading to a higher degree of local clustering of longer ligands. This is qualitatively consistent with findings from previous simulations of functionalized nanoparticles[20–22] and further supports the role of hydrophobic packing that promotes asymmetric distribution of long surface ligands. Due to the charged nature of quaternary amine ligands, however, the degree of "ligand bundling" is minimal compared to previous studies of nanoparticles functionalized with charge-neutral ligands.[20,22] The difference between the current explicit solvent simulations and previous implicit solvent simulations[17] further highlights the importance of treating solvent and ions carefully at the nanoparticle/solvent interface.[26,55–57] The diverse environment experienced by the head groups of long ligands due to clustering is qualitatively consistent with the significant difference between T_2 and T_2^* observed experimentally.[17]

On the other hand, due to the considerable flexibility of long ligands such as MTAB, the local clustering of long ligands is not long-lived and rearranges at the time scale of one to ten nanoseconds, as revealed by the computed van Hove functions and spherical Voronoi tessellation. The relatively fast ligand dynamics is also characterized by the head group methyl proton P_2 autocorrelation functions, which point to at least two decay time scales with the longer one on the scale of merely hundreds of picoseconds. Therefore, the structure of surface ligands are generally highly dynamical and expected to form only transient structural features that nevertheless can be taken advantage of in certain applications.[10] The short time scale for the rearrangements of ligand conformation suggests that they are unlikely to represent the kinetic bottleneck for nanoparticle-(bio)molecular interactions.

Compared to the ligands on curved surfaces, MTABs on the gold slab are observed to feature less spatial clustering in the simulations as expected based on packing argument. For the same reason, MTABs on a flat surface are observed to remain better correlated in time and exhibit less flexibility, as revealed by the computed van Hove functions. As a result, they actually exhibit somewhat broader distributions of methyl proton reorientation time scales and order parameters than MTABs on the surface of small nanoparticles.

In general, the simulations are consistent with the recent NMR relaxation study, which pointed to a higher degree of spatial heterogeneity for MTAB ligands on smaller nanoparticles than on larger ones. The computed T_2 relaxation times for the head group methyl protons compare favorably with experimental data, which provide essential validation to the nanoparticle model and the simulation protocol. However, we note that the T_2 relaxation time becomes dominated by the overall rotational relaxation and insensitive to the time scales of ligand dynamics for nanoparticles larger than 3 nm (hydrodynamic radius). This highlights the importance of studying small nanoparticles for characterizing ligand dynamics (i.e., τ_s), although surface features such as ligand flexibility and heterogeneity can be qualitatively reflected through order parameters and T_2/T_2^* comparison in the case of larger particles. Moreover, quantitative simulations of small nanoparticles are more feasible compared to much larger ones (e.g., those with core radius beyond 10 nm), thus particles with radii in the range of a few nanometers are better suited for integrated experimental/computational analyses aimed at an atomistic level of understanding.[9,10,38]

Finally, our simulations show that the conformational properties of surface ligands have a significant impact on the electrostatic properties of the nanoparticle. Somewhat counterintuitively, nanoparticles functionalized with longer ligands exhibit *higher* electrophoretic mobilities than the particle decorated with shorter ligands, an observation further highlighting the role of counter ions at the nanoparticle/solvent interface.[26,55] Since interfacial electrostatic properties are expected to contribute to the binding of (bio)molecules with nanoparticles, our observation suggests that nano/bio interactions can be modulated by perturbing the conformational ensemble of surface ligands, which again underscores the importance of understanding factors that control the surface ligand conformation and dynamics.

Acknowledgement

This material is based upon work supported by the National Science Foundation under Grant No. CHE-2001611, the NSF Center for Sustainable Nanotechnology (CSN). The CSN is part of the Centers for Chemical Innovation Program. Computational resources from the Extreme Science and Engineering Discovery Environment (XSEDE), which is supported by NSF grant number OCI-1053575, are greatly appreciated; part of the computational work was performed on the Shared Computing Cluster which is administered by Boston University's Research Computing Services (URL: www.bu.edu/tech/support/research/).

Supporting Information Available

Additional analyses of spatial ligand distributions, methyl proton dynamics and T_2 relaxation times, drift velocity simulations and apparent charge profiles are included. This material is available free of charge via the Internet at `http://pubs.acs.org/`.

References

(1) Barrat, J.-L.; Hansen, J.-P. *Basic concepts for simple and complex liquids*; Cambridge University Press, 2003.

(2) Zhang, Y. Q.; Tamijani, A. A.; Taylor, M. E.; Zhi, B.; Haynes, C. L.; Mason, S. E.; Hamers, R. J. Molecular surface functionalization of carbon materials via radical-induced grafting of terminal alkenes. *J. Am. Chem. Soc.* **2019**, *141*, 8277–8288.

(3) Gittins, D.; Caruso, F. Tailoring the polyelectrolyte coating of metal nanoparticles. *J. Phys. Chem. B* **2001**, *105*, 6846–6852.

(4) Murphy, C. J.; Vartanian, A. M.; Geiger, F. M.; Hamers, R. J.; Pedersen, J.; Cui, Q.; Haynes, C. L.; Carlson, E. E.; Hernandez, R.; R. D. Klaper et al., Biological Responses

to Engineered Nanomaterials: Needs for the Next Decade. *ACS Central Sci.* **2015**, *1*, 117–123.

(5) Payne, C. K. A protein corona primer for physical chemists. *J. Chem. Phys.* **2019**, *151*, 130901.

(6) Scheepers, M. R. W.; van IJzendoorn, L. J.; Prins, M. W. J. Multivalent weak interactions enhance selectivity of interparticle binding. *Proc. Natl. Acad. Sci. USA* **2020**, *117*, doi.org/10.1073/pnas.2003968117.

(7) Luo, Z.; Marson, D.; Ong, Q. K.; Loiudice, A.; Kohlbrecher, J.; Radulescu, A.; Krause-Heuer, A.; Darwish, T.; Balog, S.; Buonsanti, R.; Svergun, D. I.; Posocco, P.; Stellacci, F. Quantitative 3D determination of self-assembled structures on nanoparticles using small angle neutron scattering. *Nat. Comm.* **2018**, *9*, 1343.

(8) Luo, Z.; Zhao, Y. F.; Darwish, T.; Wang, Y.; Hou, J.; Stellacci, F. Mass spectrometry and Monte Carlo method mapping of nanoparticle ligand shell morphology. *Nat. Comm.* **2018**, *9*, 4478.

(9) Salorinne, K.; Malola, S.; Wong, O. A.; Rithner, C. D.; Chen, X.; Ackerson, C. J.; Hakkinen, H. Conformation and dynamics of the ligand shell of a water-soluble Au-102 nanoparticle. *Nat. Comm.* **2016**, *7*, 10401.

(10) Riccardi, L.; Gabrielli, L.; Sun, X. H.; De Biasi, F.; Rastrelli, F.; Mancin, F.; De Vivo, M. Nanoparticle-Based Receptors Mimic Protein- Ligand Recognition. *Chem.* **2017**, *3*, 92–109.

(11) Zhang, Y. Q.; Fry, C. G.; Pedersen, J. A.; Hamers, R. J. Dynamics and morphology of nanoparticle-linked polymers elucidated by NMR. *Anal. Chem.* **2017**, *89*, 12399–12407.

(12) Chong, G.; Hernandez, R. Adsorption dynamics and structure of polycations on citrate-coated gold nanoparticles. *J. Phys. Chem. C* **2018**, *122*, 19962–19969.

(13) Netz, R. R.; Andelman, D. Neutral and charged polymers at interfaces. *Phys. Rep.* **2003**, *380*, 1–95.

(14) Dobrynin, A. V.; Rubinstein, M. Theory of polyelectrolytes in solutions and at surfaces. *Prog. Poly. Sci.* **2005**, *30*, 1049–1118.

(15) Hens, Z.; Martins, J. C. A Solution NMR Toolbox for Characterizing the Surface Chemistry of Colloidal Nanocrystals. *Chem. Mater.* **2013**, *25*, 1211–1221.

(16) Cui, Q.; Hernandez, R.; Mason, S. E.; Frauenheim, T.; Pedersen, J. A.; Geiger, F. Sustainable nanotechnology: opportunities and challenges for theoretical/computational studies. *J. Phys. Chem. B* **2016**, *120*, 7297–7306.

(17) Wu, M.; Vartanian, A. M.; Chong, G.; Pandiakumar, A. K.; Hamers, R. J.; Hernandez, R.; Murphy, C. J. Solution NMR Analysis of Ligand Environment in Quaternary Ammonium-Terminated Self-Assembled Monolayers on Gold Nanoparticles: The Effect of Surface Curvature and Ligand Structure. *J. Am. Chem. Soc.* **2019**, *141*, 4316–4327.

(18) Chong, G.; Foreman-Ortiz, I. U.; Wu, M.; Bautista, A.; Murphy, C. J.; Pedersen, J. A.; Hernandez, R. Defects in Self-Assembled Monolayers on Nanoparticles Prompt Phospholipid Extraction and Bilayer-Curvature-Dependent Deformations. *J. Phys. Chem. C* **2019**, *123*, 27951–27958.

(19) Tu, Y. S.; Lv, M.; Xiu, P.; Huynh, T.; Zhang, M.; Castelli, M.; Liu, Z. R.; Huang, Q.; Fan, C. H.; H. P. Fang et al., Destructive extraction of phospholipids from Escherichia coli membranes by graphene nanosheets. *Nat. Nanotech.* **2013**, *8*, 594–601.

(20) Ghorai, P. K.; Glotzer, S. C. Molecular Dynamics Simulation Study of Self-Assembled Monolayers of Alkanethiol Surfactants on Spherical Gold Nanoparticles. *J. Phys. Chem. C* **2007**, *111*, 15857–15862.

(21) Bolintineanu, D. S.; Lane, J. M. D.; Grest, G. S. Effects of Functional Groups and Ionization on the Structure of Alkanethiol-Coated Gold Nanoparticles. *Langmuir* **2014**, *30*, 11075–11085.

(22) Chew, A. K.; R. C. van Lehn, Effect of Core Morphology on the Structural Asymmetry of Alkanethiol Monolayer-Protected Gold Nanoparticles. *J. Phys. Chem. C* **2018**, *122*, 26288–26297.

(23) Lipari, G.; Szabo, A. Model-free approach to the interpretation of nuclear magnetic-resonance relax- ation in macromolecules .1. theory and range of validity. *J. Am. Chem. Soc.* **1982**, *104*, 4546–4559.

(24) Levy, R. M.; Karplus, M.; Wolynes, P. G. NMR relaxation parameters in molecules with internal motion: exact Langevin trajectory results compared with simplified relaxation models. *J. Am. Chem. Soc.* **1981**, *103*, 5998–6011.

(25) Villa, A.; Stock, G. What NMR relaxation can tell us about the internal motion of an RNA hairpin: A molecular dynamics simulation study. *J. Chem. Theory Comput.* **2006**, *2*, 1228–1236.

(26) Liang, D. Y.; Dahal, U.; Zhang, Y. Q.; Lochbaum, C.; Hamers, R. J.; Pedersen, J. A.; Cui, Q. Interfacial water and ion distribution determine ζ-potential and binding affinity of nanoparticles to biomolecules. *Nanoscale* **2020**, *12*, 18106–18123.

(27) Schmit, J. D.; Kariyawasam, N. L.; Needham, V.; Smith, P. E. SLTCAP: A simple method for calculating the number of ions needed for MD simulation. *J. Chem. Theory Comput.* **2018**, *14*, 1823–1827.

(28) MacKerell, A. D.; Bashford, D.; Bellott, M.; Dunbrack, R. L.; Evanseck, J. D.; Field, M. J.; Fischer, S.; Gao, J.; Guo, H.; S. Ha et al., All-Atom Empirical Potential for Molecular Modeling and Dynamics Studies of Proteins. *J. Phys. Chem. B* **1998**, *102*, 3586–3616.

(29) Huang, J.; A. D. MacKerell Jr., CHARMM36 All-atom Additive Protein Force Field: Validation Based on Comparison to NMR Data. *J. Comput. Chem.* **2013**, *34*, 2135–2145.

(30) Jorgensen, W. L.; Chandrasekhar, J.; Madura, J. D.; Impey, R. W.; Klein, M. L. Comparison of simple potential functions for simulating liquid water. *The Journal of chemical physics* **1983**, *79*, 926–935.

(31) Venable, R. M.; Luo, Y.; Gawrisch, K.; Roux, B.; Pastor, R. W. Simulations of anionic lipid membranes: development of interaction-specific ion parameters and validation using NMR data. *J. Phys. Chem. B* **2013**, *117*, 10183–10192.

(32) Heinz, H.; Lin, T.-J.; Kishore Mishra, R.; Emami, F. S. Thermodynamically consistent force fields for the assembly of inorganic, organic, and biological nanostructures: the INTERFACE force field. *Langmuir* **2013**, *29*, 1754–1765.

(33) Phillips, J. C.; Braun, R.; Wang, W.; Gumbart, J.; Tajkhorshid, E.; Villa, E.; Chipot, C.; Skeel, R. D.; Kale, L.; Schulten, K. Scalable molecular dynamics with NAMD. *J. Comput. Chem.* **2005**, *26*, 1781–1802.

(34) Darden, T.; York, D.; Pedersen, L. Particle mesh Ewald: An N log (N) method for Ewald sums in large systems. *J. Chem. Phys.* **1993**, *98*, 10089–10092.

(35) Ryckaert, J.-P.; Ciccotti, G.; Berendsen, H. J. Numerical integration of the cartesian equations of motion of a system with constraints: molecular dynamics of n-alkanes. *J. Comput. Phys.* **1977**, *23*, 327–341.

(36) Brünger, A. T. *X-PLOR: version 3.1: a system for x-ray crystallography and NMR*; Yale University Press, 1992.

(37) Feller, S. E.; Zhang, Y.; Pastor, R. W.; Brooks, B. R. Constant pressure molecular

dynamics simulation: the Langevin piston method. *J. Chem. Phys.* **1995**, *103*, 4613–4621.

(38) Riccardi, L.; De Biasi, F.; De Vivo, M.; Bürgi, T.; Rastrelli, F.; Salassa, G. Dynamic Origin of Chirality Transfer between Chiral Surface and Achiral Ligand in Au38 Clusters. *ACS Nano* **2019**, *13*, 7127–7134.

(39) Levy, R. M.; Dobson, C. M.; Karplus, M. Dipolar NMR Relaxation of Nonprotonated Aromatic Carbons in Proteins. *Biophys. J.* **1982**, *39*, 107–113.

(40) McQuarrie, D. A. *Statistical Mechanics*; Harper & Row: New York, 1976.

(41) Clore, G. M.; Szabo, A.; Bax, A.; Kay, L. E.; Driscoll, P. C.; Gronenborn, A. M. Deviations from the simple two-parameter model-free approach to the interpretation of nitrogen-15 nuclear magnetic relaxation of proteins. *J. Am. Chem. Soc.* **1990**, *112*, 4989–4991.

(42) Doane, T. L.; Chuang, C.-H.; Hill, R. J.; Burda, C. Nanoparticle ζ-potentials. *Acc. Chem. Res.* **2011**, *45*, 317–326.

(43) Lowry, G. V.; Hill, R. J.; Harper, S.; Rawle, A. F.; Hendren, C. O.; Klaessig, F.; Nobbmann, U.; Sayre, P.; Rumble, J. Guidance to improve the scientific value of zeta-potential measurements in nanoEHS. *Environ. Sci-Nano* **2016**, *3*, 953–965.

(44) Zhang, Y.; Fry, C. G.; Pedersen, J. A.; Hamers, R. J. Dynamics and morphology of nanoparticle-linked polymers elucidated by nuclear magnetic resonance. *Anal. Chem.* **2017**, *89*, 12399–12407.

(45) Yeh, I.-C.; Hummer, G. Diffusion and electrophoretic mobility of single-stranded RNA from molecular dynamics simulations. *Biophys. J* **2004**, *86*, 681–689.

(46) Ge, Z.; Wang, Y. Estimation of Nanodiamond Surface Charge Density from Zeta Potential and Molecular Dynamics Simulations. *J. Phys. Chem. B* **2016**, *121*, 3394–3402.

(47) Batty, M. Spatial Entropy. *Geographical analysis* **1974**, *6*, 1–31.

(48) Virtanen, P.; Gommers, R.; Oliphant, T. E.; Haberland, M.; Reddy, T.; Cournapeau, D.; Burovski, E.; Peterson, P.; Weckesser, W.; J. Bright et al., SciPy 1.0: fundamental algorithms for scientific computing in Python. *Nat. Methods* **2020**, *17*, 261–272.

(49) Hansen, J.-P.; McDonald, I. R. *Theory of Simple Liquids*; Academic Press: London, 2006.

(50) Kubo, R.; Toda, M.; Hashitsume, N. *Statistical Physics II: Nonequilibrium Statistical Mechanics*; Springer: New York, 2003.

(51) Hunter, R. J. *Zeta potential in colloid science: principles and applications*; Academic press, 2013; Vol. 2.

(52) Walker, D. A.; Kowalczyk, B.; de la Cruz, M. O.; Grzybowski, B. A. Electrostatics at the nanoscale. *Nanoscale* **2011**, *3*, 1316–1344.

(53) Hong, J.; Hamers, R. J.; Pedersen, J. A.; Cui, Q. A hybrid molecular dynamics/multiconformer continuum electrostatics (MD/MCCE) approach for the determination of surface charge of nanomaterials. *J. Phys. Chem. C* **2017**, *121*, 3584–3596.

(54) De Roo, J.; Yazdani, N.; Drijvers, E.; Lauria, A.; Maes, J.; Owen, J. S.; Van Driessche, I.; Niederberger, M.; Wood, V.; J. C. Martins et al., Probing Solvent-Ligand Interactions in Colloidal Nanocrystals by the NMR Line Broadening. *Chem. Mater.* **2018**, *30*, 5485–5492.

(55) Breier, L. B.; Nagata, Y.; Lutz, H.; Gonella, G.; Hunger, J.; Backus, E. H. G.; Bonn, M. Saturation of charge-induced water alignment at model membrane surfaces. *Sci. Adv.* **2018**, *4*, eaap7415.

(56) Luo, Z.; Murello, A.; Wilkins, D. M.; Kovacik, F.; Kohlbrecher, J.; Radulescu, A.; Okur, H. I.; Ong, Q. K.; Roke, S.; M. Ceriotti et al., Determination and evaluation of

the nonadditivity in wetting of molecularly heterogeneous surfaces. *Proc. Natl. Acad. Sci. USA* **2019**, *116*, 25516–25523.

(57) Batista, C. A. S.; Larson, R. G.; Kotov, N. A. Nonadditivity of Nanoparticle Interactions. *Science* **2015**, *350*, 1242477.

Graphical TOC Entry